PAPER

Magnetic structure and exchange interactions in pyrrhotite end member minerals: hexagonal FeS and monoclinic Fe_7S_8

IOP Publishing Journal of Physics: Condensed Matter
J. Phys.: Condens. Matter **33** (2021) 465801 (10pp) https://doi.org/10.1088/1361-648X/ac1cb2

Magnetic structure and exchange interactions in pyrrhotite end member minerals: hexagonal FeS and monoclinic Fe_7S_8

Aleksandar Živković[1,*], Helen E King[1], Mariette Wolthers[1] and Nora H de Leeuw[1,2,*]

[1] Department of Earth Sciences, Utrecht University, Princetonlaan 8a, 3584CB Utrecht, The Netherlands
[2] School of Chemistry, University of Leeds, Woodhouse Lane, Leeds LS2 9JT, United Kingdom

E-mail: A.Zivkovic@uu.nl and N.H.deLeeuw@uu.nl

Received 28 June 2021, revised 6 August 2021
Accepted for publication 11 August 2021
Published 3 September 2021

Abstract

Iron mono-sulphides, or pyrrhotites, are minerals present in the Earth's crust and mantle as well as major magnetic constituents of several classes of meteorites, thus are of interest to a wide range of disciplines including geology, geophysics, geochemistry, and material science. Despite displaying diverse magnetic properties as a result of iron vacancy ordering, the underlying exchange mechanism has not been quantified. This study presents an examination of the electronic and magnetic properties for the two pyrrhotite group end members, hexagonal FeS and monoclinic Fe_7S_8 (4C superstructure) by means of density functional theory coupled with a Heisenberg magnetic model. The easy magnetization axes of FeS and Fe_7S_8 are found to be positioned along the crystallographic c-direction and at an angle of 56° to the c-direction, respectively. The magnetic anisotropy energy in Fe_7S_8 is greatly increased as a consequence of the vacancy framework when compared to FeS. The main magnetic interaction, in both compounds, is found to be the isotropic exchange interaction favouring antiferromagnetic alignment between nearest-neighbouring spins. The origin of the exchange interaction is elucidated further following the Goodenough–Kanamori–Anderson rules. The antisymmetric spin exchange is found to have a minor effect in both compounds. The theoretical findings presented in this work thus help to further resolve some of the ambiguities in the magnetic features of pyrrhotites.

Keywords: troilite FeS, pyrrhotite 4C Fe_7S_8, exchange interaction, magnetic anisotropy energy, Heisenberg magnetic model, density functional theory

(Some figures may appear in colour only in the online journal)

1. Introduction

The pyrrhotite group encompasses a wide range of natural and synthetic iron-sulphur phases with the generic formula $Fe_{1-x}S$, where x is between $0 \leqslant x \leqslant 0.125$ and a crystal structure of the NiAs type [1–3]. Stoichiometric FeS ($x = 0$) is known as troilite and has a hexagonal NiAs-type structure. Stoichiometry alterations introduced via different arrangements of iron vacancies form variable pyrrhotite superstructures. The numerous pyrrhotite superstructures are sorted into five categories according to their multiplicities of the NiAs sublattice: (i) 2C for troilite, (ii) 4C for monoclinic pyrrhotite, (iii) NC ($a = 2$A; $c = N$C, N varies continuously between 5.0 and 11.0), (iv) MC ($a = 2$A, $c = M$C, M varies between 3.0 and 4.0), and

* Authors to whom any correspondence should be addressed.

(v) NA ($a = N$A; $c = 3$C, N varies between 40 and 90), where A and C are the respective NiAs sub cell lattice parameters [4, 5].

Pyrrhotites are of interest to both condensed matter and planetary sciences owing to geophysical arguments suggesting that they are a possible component of the interior of terrestrial planets such as the Earth or Mars and are a common mineral in lunar and meteorite samples. Furthermore, pyrrhotite is the only binary sulphide common enough to be considered a rock-forming mineral [6–8]. In addition, pyrrhotites have been synthesised experimentally in low-temperature aqueous systems, including in the presence of bacteria indicating that they can be produced via biological processes [9].

The present study concerns the two end members of this particular iron monosulphide group, namely FeS (hexagonal troilite, 2C superstructure) and Fe_7S_8 (monoclinic pyrrhotite, 4C superstructure). FeS is an antiferromagnet (AFM) below the Néel temperature of $T_N = 592$–598 K. Although above 420 K FeS is a metal, below this temperature it has a narrow band gap of around 0.04 eV and thus behaves as an insulator [10]. Fe_7S_8 is a metal with a Néel temperature of $T_N = 578$ K, in which the sulphur content is slightly greater than in FeS. It contains eight molecular units of Fe_7S_8 in the unit cell and has a ferrimagnetic (FIM) ordering originating from the relative arrangement of the vacant sites and iron atoms [1, 11].

The magnetic features of FeS and Fe_7S_8 have been explored to a moderate extent over the last decades. Early studies by Sato [12] measured the anisotropy energy for natural Fe_7S_8 samples and noted that the easy direction of magnetization lies between the crystallographic c-axis and c-plane. Levinson *et al* [13] conducted Mössbauer measurements on laboratory-prepared specimen of Fe_7S_8 with and without the presence of an applied external magnetic field. They noted a lack of trivalent iron atoms in their spectra, indicating that the ionic model of $(Fe^{3+})_2(Fe^{2+})_5(S^{2-})_8$ may rather correspond to a charge state of $(Fe^{2.28+})_7(S^{2-})_8$, suggesting itinerant rather than localized electronic behaviour in this system. Shimada *et al* [10] studied the electronic structures of FeS, Fe_7S_8, and Fe_7Se_8 using photoemission and inverse-photoemission spectroscopy, confirming FeS as an AFM semiconductor and Fe_7S_8 as an FIM metal. The change from the AFM insulator FeS to the FIM metal Fe_7S_8 was viewed from two standpoints: band picture and hole doping. In the first one the introduced Fe vacancies causes a decrease in the filling of the Fe 3d band as a result of the large number of removed electrons compared to the removed Fe 3d states. In the second picture, hole doping into the Mott insulator FeS occurs through Fe vacancies where the lower Hubbard band is shifted towards the E_F and the spectral weight transferred to above the E_F, effectively filling the band gap of FeS. Powell *et al* [14] used neutron diffraction to probe the structure and magnetism of Fe_7S_8. They found that the crystallographic and magnetic unit cells are coincident with a magnetic propagation vector $\mathbf{k} = (0, 0, 0)$. Also, the magnetic moments measured at 11 K were found to be directed at an angle of 29° to the layers of iron.

More recent works have dealt mostly with the low temperature magnetic transition around 30 K also known as the Besnus transition, which is considered to allow the easy detection of the mineral in natural samples [15–21]. William Herbert *et al* [22] conducted diffusion measurements in $Fe_{1-x}S$ as a function of temperature in the range 170 °C–400 °C. The measured activation energy for diffusion in the paramagnetic and structurally disordered pyrrhotite was 0.83 eV, which was found substantially lower compared to the activation energy of 1.18–1.30 eV in the fully magnetic ordered state. This was the first description of a magnetic diffusion anomaly in an ionic compound or FIM material. Soon after, this behaviour was complemented with kinetic Monte-Carlo and DFT studies [23]. Furthermore, $Fe_{1-x}S$ nano-wires and nano-disks that display a particular type of AFM to FIM transition upon heating have been investigated and proposed for technological purposes such as phase-change magnetic memory devices [23–25]. Overall, pyrrhotites have attracted a considerable interest in fundamental magnetism over the past decades as a result of the diverse magnetic properties displayed through the iron deficiency coupled with many existing superstructures [20].

Earlier theoretical investigations of troilite and pyrrhotite included a variety of techniques to explore their ground state properties, such as LAPW + LDA [26], Hartree–Fock [27], density functional theory (DFT) [28–30], and LMTO + LSDA [31]. Ushakov *et al* [32] performed DFT + DMFT calculations on FeS under pressure. They found that under normal conditions FeS orders magnetically with Fe ions adopting a single ionic configuration and via this behaviour they explained why LDA + U calculations are able to reproduce the band gap and experimental photoemission spectra of FeS. In contrast, under higher pressures static mean-field methods (like LDA + U) were found to break down and advanced techniques such as DMFT are essential.

Despite the considerable effort dedicated to the understanding of magnetic properties in FeS and Fe_7S_8, a complete and solid quantification of the magnetic exchange coupling in these materials is still missing. In order to shed light on these phenomena, in this work, calculations based on DFT have been employed, together with a microscopic Heisenberg model that includes the superexchange and Dzyaloshinskii–Moriya (DM) interactions between the magnetic atoms in FeS and Fe_7S_8. By employing the method outlined below to obtain the exchange interactions, we are not limited to exchange interactions between nearest neighbours or next nearest neighbours only but can obtain the relevant interactions across the whole simulation cell. The following questions are addressed: (i) what is the origin of exchange coupling in FeS and Fe_7S_8 and (ii) how does the exchange coupling differ across the two systems with increasing content of iron vacancies?

2. Computational details

Spin-polarized DFT calculations were performed using the Vienna *ab initio* simulation package (VASP v5.4.4) [33–35] with the projector-augmented wave (PAW) method and a plane-wave cutoff of 400 eV. For the PAW potentials, the valence electronic configurations used were $4s^1 3d^7$ for iron and $3s^2 3p^4$ for sulphur. The general gradient approximation (GGA) for the exchange-correlation (XC) functional

was employed with the Perdew–Burke–Ernzerhof (PBE) parametrization [36] for DFT + U calculations within the formalism of Dudarev *et al* [37]. For FeS troilite, the $U_{\text{eff}} = U - J = 1$ eV value was taken from earlier works [38], while the U_{eff} for Fe_7S_8 pyrrhotite was tuned as described below, with a final utilized value of $U_{\text{eff}} = U - J = 1.5$ eV. Long distance dispersion corrections were included using the D3 approach of Grimme *et al* [39]. Non-collinear magnetism has been performed by including spin–orbit coupling (SOC) effects.

The conjugate gradient method was used for structural optimisations, with the total energy and force convergence criteria set to 10^{-5} eV and 0.01 eV Å^{-1}, respectively. The Brillouin zone was sampled using $2 \times 5 \times 2$ and $7 \times 7 \times 5$ Γ-centred Monkhorst–Pack meshes for Fe_7S_8 and FeS troilite, respectively [40], while the partial occupancies were determined using the method of Methfessel–Paxton with a set width for all calculations of 0.01 eV. The extent of charge distributions was studied using the Bader scheme as implemented in the Henkelman code [41–43]. Graphical drawings were produced using VESTA [44].

The magnetic anisotropy energy (MAE) was determined using the so-called magnetic force theorem [45, 46], by performing fully self-consistent calculations for the collinear case and subsequently freezing the potential charge density for different orientations of the magnetization direction and then taking the energy differences with respect to the minimal energy configuration. Convergence of the MAE energy of about 0.1 μeV atom^{-1} was achieved using 325 k points for Fe_7S_8 and 245 k points for FeS over the complete Brillouin zone. The convergence tests have been performed for up to 637 k points for Fe_7S_8 and 567 k points for FeS.

Starting from DFT, the Hamiltonian in the basis of the Wannier functions (WFs) was constructed using the Wannier90 code (v3.1.0) [47–50]. To build the actual WFs and calculate the maximally localized Wannier functions (MLWFs), an updated VASP2WANNIER90 interface was used in order to correctly account for the projections when SOC effects are included[1]. To obtain the magnetic interaction parameters, the TB2J package was used [51]. The orbitals included to construct the Hamiltonian in the basis of the WFs were the Fe-3d and S-3p states. The spread of the 3d orbitals and 3p orbitals was converged to less than 1 Å^2 and 2 Å^2, respectively. The spin Heisenberg Hamiltonian employed through the TB2J package reads as:

$$E = -\sum_i K_i \vec{S}_i^2 - \sum_{i \neq j} \left[J_{ij}^{\text{iso}} \vec{S}_i \cdot \vec{S}_j + \vec{S}_i \mathrm{J}_{ij}^{\text{iso}} \vec{S}_j + \vec{D}_{ij} \cdot \left(\vec{S}_i \times \vec{S}_j \right) \right].$$

The first term represents the single-ion anisotropy, the second the isotropic exchange, the third the symmetric anisotropic exchange, and the last term the DM interaction. The convention used within this framework is that positive exchange J values favour ferromagnetic spin alignment. Each pair ij is counted twice and the spin vectors are normalized to 1, to yield parameters in the units of energy.

[3] https://github.com/Chengcheng-Xiao/VASP2WAN90_v2_fix

3. Results and discussion

3.1. Structural and electronic properties of FeS and Fe_7S_8

Troilite FeS crystallizes in a hexagonal structure (space group P-62c, no. 190), with the unit cell containing 24 atoms, 12 of each chemical species. There are only four non-equivalent positions in the cell (occupied by one iron and three sulphur), with sulphur atoms situated at the vertices of an octahedron around each iron atom. The calculated lattice parameters of FeS read $a = b = 5.898$ Å and $c = 11.593$ Å, which is in agreement with earlier theoretical works [30] as well as available experimental data ($a = b = 5.965$ Å and $c = 11.759$ Å [52]).

In contrast, pyrrhotite Fe_7S_8 adopts a monoclinic structure (space group $C2/c$, no. 15), where the loss of symmetry due to the presence of defects results in a much larger unit cell that contains 60 atoms: 28 of iron and 32 of sulphur. Within the unit cell of pyrrhotite, there are eight non-equivalent positions (four iron and four sulphur sites), with each iron six-fold coordinated with sulphur atoms. The iron full and iron-deficient layer stack alternatively along the direction perpendicular to these layers.

The calculated lattice parameters and unit cell volume of Fe_7S_8 are shown in figure 1, with the final values of $a = 11.796$ Å, $b = 6.872$ Å, $c = 12.878$ Å (experimental reference values taken as $a = 11.866$ Å, $b = 6.848$ Å, $c = 12.895$ Å from [14]). Despite Fe_7S_8 exhibiting a metallic ground state, a standard GGA (PBE) functional is not sufficient to reproduce the structure correctly and underestimates the volume by more than 15% when compared to available experimental values. This discrepancy is attributed to the well-known delocalization of d and f electrons by semi-local XC functionals as well as strong electron correlations [55]. However, an additional on-site interaction to the PBE functional remedies the shortcoming and the structural parameters are recovered within less than 1% deviation. A value of $U_{\text{eff}} = 1.5$ eV applied on the Fe-d orbitals was found to yield results in almost perfect agreement with experimental values. Furthermore, adding dispersion interactions was found crucial, as otherwise the lattice b and c dimensions remain poorly described within DFT + U. With the correctly reproduced lattice parameters, the (spin only) magnetic moment present at the Fe sites is recovered as well, as depicted in figure 2. The calculated values compared well with the experimental data (see table 1).

Figures 3 and 4 depict the spin-projected electronic band structure and accompanying densities of states (DOS) of troilite and pyrrhotite. In addition, on top of the single particle Kohn–Sham electronic band structure, the interpolated band structure obtained from the subspace spanned by the minimized MLWFs is shown. The overlap between the band structures is very good, ensuring that the WFs are well localized and that their spread is minimal. An indirect gap of 0.56 eV was obtained for FeS, which overestimates the experimental value by an order of magnitude (0.04 eV [38]), yet such behaviour has been noted before and its cause discussed in previous works [30, 38, 56]. Fe_7S_8 was found to exhibit metallic behaviour due to states present at the Fermi level,

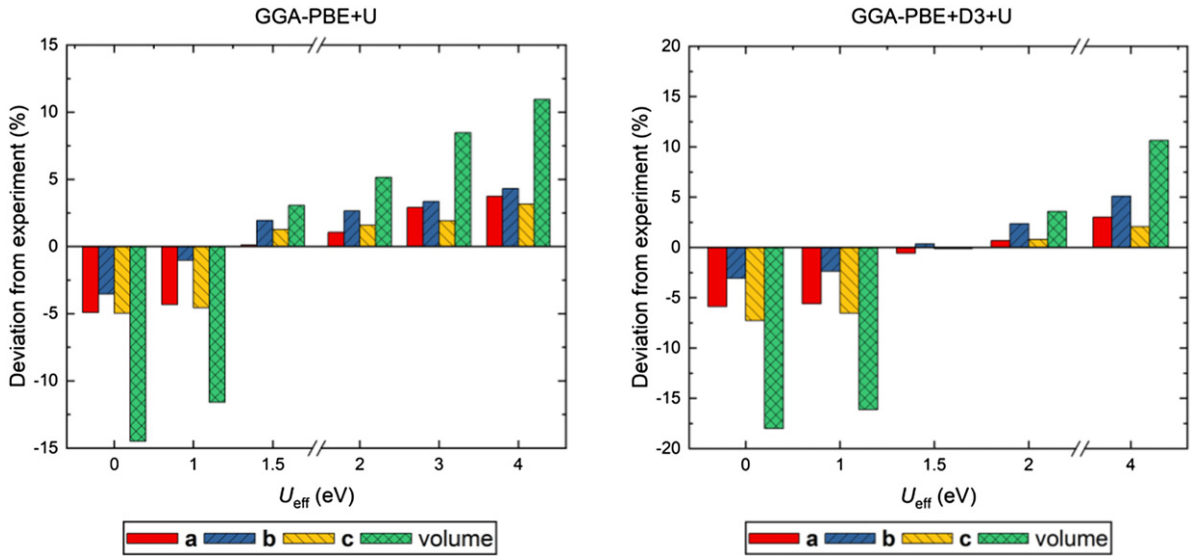

Figure 1. Calculated structural parameters and unit cell volume of Fe_7S_8 for varying U_{eff} values without (left) and with (right) additional dispersion corrections. Reference structure taken from Powell *et al* [14].

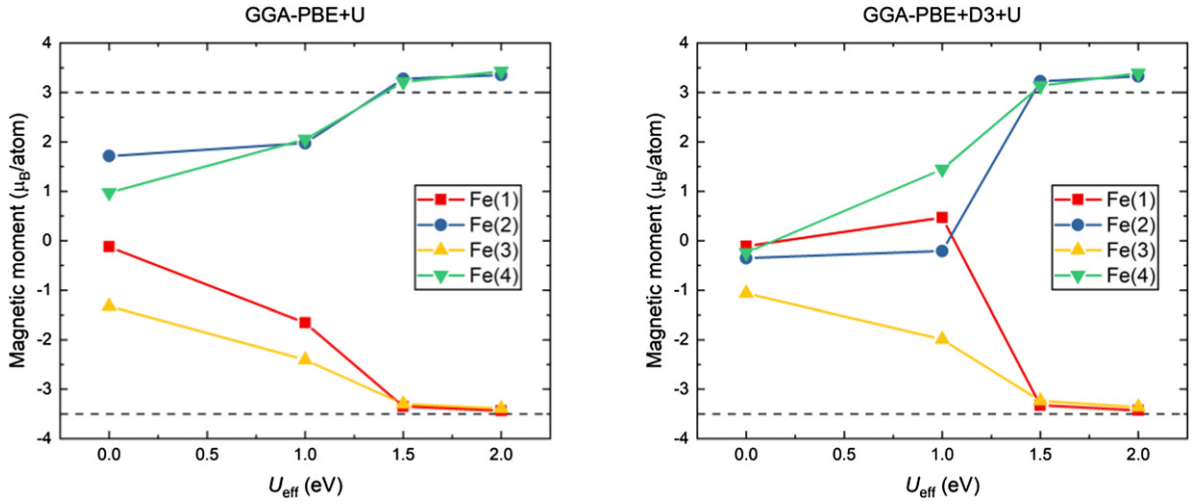

Figure 2. Calculated magnetic moment localized on the four distinct iron sites present in Fe_7S_8 for varying U_{eff} values without (left) and with (right) additional dispersion corrections. Reference magnetic moments indicated with the dashes line were taken from Powell *et al* [14].

Table 1. Spin magnetic moments for FeS and Fe_7S_8 computed with DFT + U.

	Magnetic moment (μ_B atom^{-1})	
	Experimental values	This work
Troilite FeS	3.21 [28], 4 [53]	3.04
Pyrrhotite Fe_7S_8	3.03 (at 77 K) and 3.53 (at 4.2 K) [54], 3.16 [14]	3.13–3.32

corresponding well to available experimental data which measures pyrrhotite as a highly conducting material [57].

In FeS, the Fe ions adopt a d^6 high spin configuration with a single electron in the minority spin channel in the d_{xy} orbital [32]. The calculated DOS confirm further hybridization (covalency) of Fe-3d states with the 3p orbitals of sulphur (full DOS not shown). The t_{2g} and e_g electrons at the Fe site are broadened across the whole energy range from −8 eV up to the Fermi level, which does not allow crystal field splitting to be noted, as shown in figure 4. This reflects the local irregular octahedral environment surrounding the Fe atom, where each Fe–S bond is distorted and has dissimilar bond lengths.

A similar situation is found in Fe_7S_8, with the t_{2g} and e_g electronic levels not distinctly separated but delocalized across a wide energy range. Fe is predominantly in the $3d^6$ high spin state, similar to FeS and hybridizes with the sulphur 3p states.

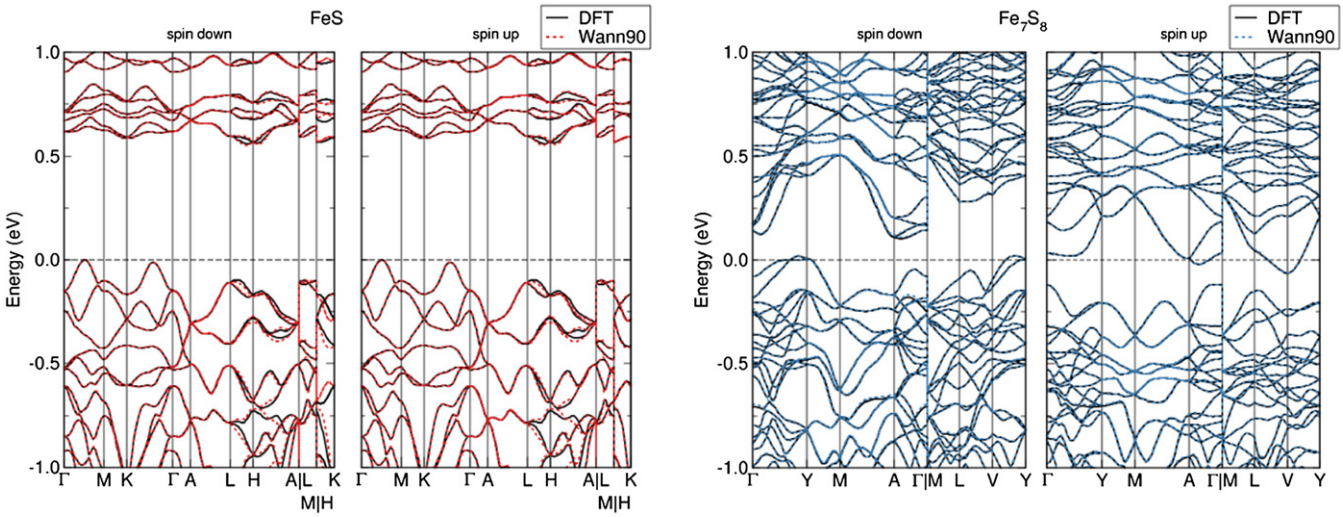

Figure 3. Electronic band structure of FeS troilite and Fe_7S_8 pyrrhotite along high-symmetry points in the Brillouin zone, calculated with for collinear spins with DFT + U.

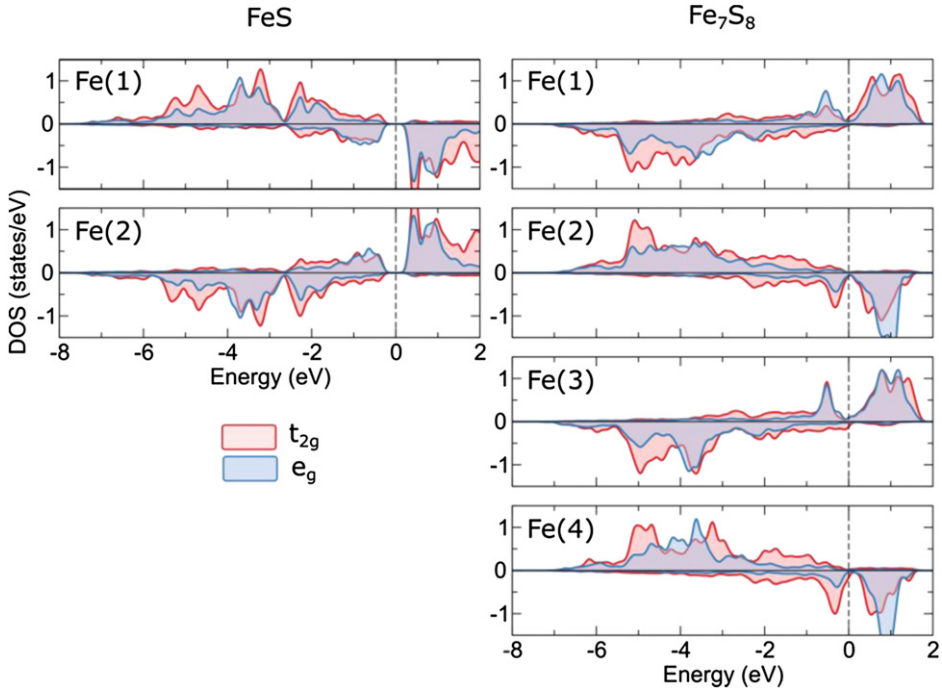

Figure 4. Orbital resolved (Fe-*d*) electronic densities of state of FeS troilite and Fe_7S_8 pyrrhotite, calculated using DFT + U.

The states around the Fermi level originate from the single electron present in the minority spin channel of each Fe atom, which stack alternately along the *c*-axis.

3.2. Magnetic anisotropy energy

The dependence of the MAE on the crystallographic directions in FeS and Fe_7S_8 is shown in figure 5. For FeS, the maximum MAE is noted for a 90° rotation from the c-axis into the *ab*-plane with a value of almost 395.9 μeV cell^{-1} (around 16.5 μeV atom^{-1}). Thus, the magnetic moments align along the *c*-axis in an AFM manner, confirming previous low temperature experimental studies of FeS [58]. For Fe_7S_8, the calculated MAE minimum is noted at a 56° angle to the c-axis (34° to the iron layers), which matches the measurements done by Powell *et al* [14], who observed that the moments are directed at ca. 29° to the iron layers at 11 K. The MAE in Fe_7S_8 due to SOC reads 5488.5 μeV cell^{-1} (around 91.5 μeV atom^{-1}), which is greatly enlarged in magnitude compared to FeS. This is a direct consequence of the symmetry reduction from a hexagonal to monoclinic structure and subsequent increase of Fe–Fe orbital overlap, as postulated by Koulialias *et al* [59].

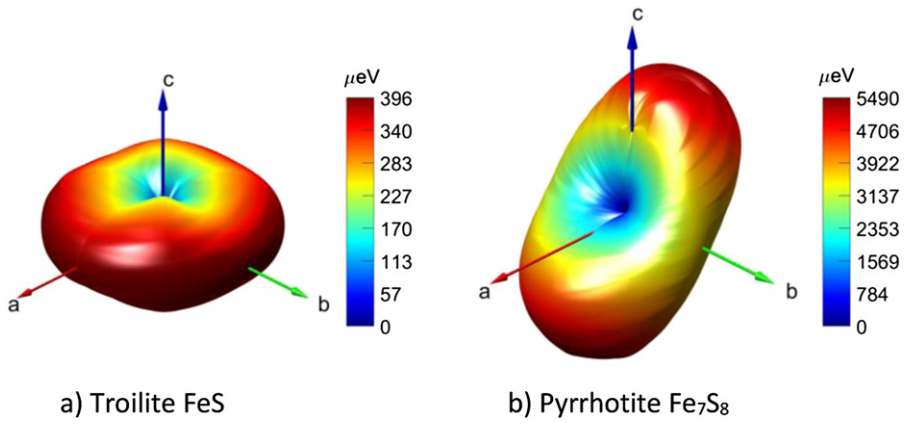

Figure 5. Magnetic anisotropy energy per unit cell for troilite FeS (left) and pyrrhotite Fe_7S_8 (right) obtained with DFT + U.

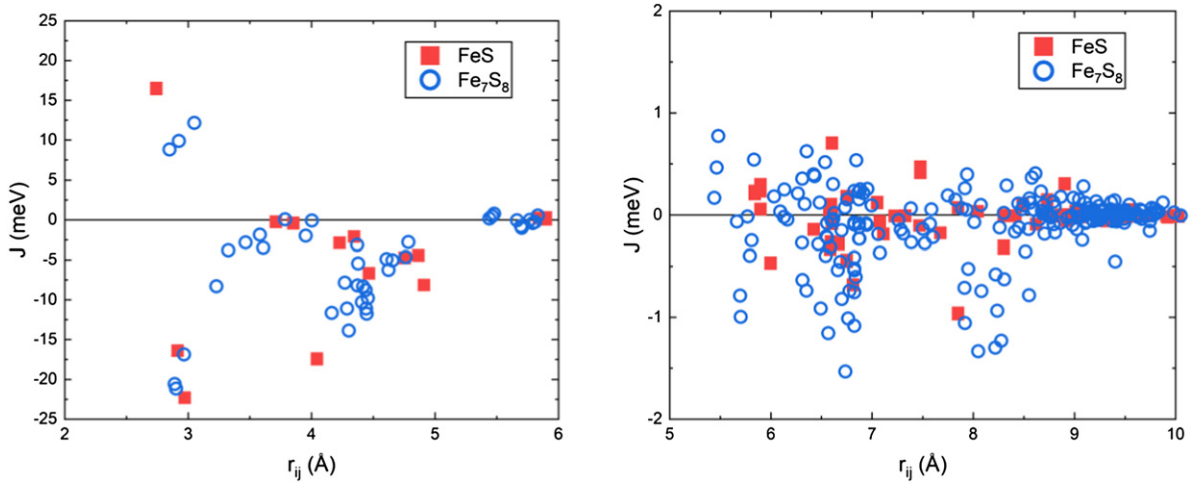

Figure 6. Calculated magnetic interaction parameters from DFT + U of FeS and Fe_7S_8 as a function of interatomic distance.

3.3. Exchange parameters

The DFT + U results of the exchange interaction parameters between Fe atoms at different sites in FeS and Fe_7S_8 are shown in figure 6. For FeS, only one ferromagnetic exchange interaction between iron atoms of the same spin state in the *ab*-plane is identified, with a magnitude of 16.5 meV (denoted as J_1, for detailed visualization see figure 7). The strongest magnetic interaction ($J_3 = -22.2$ meV) is AFM between Fe atoms separated at $d = 2.972$ Å on top of each other along the *c*-axis. The superexchange interactions occurring between Fe–Fe atoms placed further than 5.5 Å apart are an order of magnitude weaker than the direct exchange and demonstrate competitive interplay between ferromagnetic and AFM behaviour.

The observed magnetic behaviour in FeS can be elucidated following the Goodenough–Kanamori–Anderson (GKA) rules [60–65]. The favourable Fe–Fe distance of atoms stacked along the crystallographic c-direction of less than 3 Å enables effective *d* orbital overlap without ligand (sulphur, *p* orbital) participation. Furthermore, the Fe centres lie on top of one another so that the half-filled *d* orbitals are directed towards each other enabling effective spin hopping between them. This arrangement explains the origin of the AFM interaction between adjacent spin-alternating Fe layers. The FM interacting iron atoms occupy every other corner of the hexagon formed in the *ab*-plane. Such a geometry and distances of 2.743 Å allow for orbital overlap which minimizes the intra-site Coulomb energy and maximizes the spin multiplicity, favouring FM coupling.

Similar magnetic behaviour to that of FeS is noted for Fe_7S_8. Due to symmetry reduction in Fe_7S_8, the FM exchange interaction is no longer uniquely defined. Obtained values are in the range of 8.7–12.3 meV as a result of the variable intralayer Fe–Fe distance of 2.849 Å–3.050 Å (along the crystallographic *c*-direction, grouped as the J_c interaction in figure 7). Compared to FeS, the FM interaction is weakened as a consequence of the extended intralayer Fe–Fe bond length, in accordance with the aforementioned GKA rules. The dominant magnetic interaction in Fe_7S_8 remains AFM and does not experience substantial magnitude reduction, compared to FeS, with a maximal value of −21.2 meV (labelled as J_a, d(Fe–Fe) = 2.892 Å). The superexchange interaction between magnetic Fe sites in Fe_7S_8 is somewhat enhanced compared to FeS, yet the values remain for one order of magnitude lower than the dominant exchange interaction.

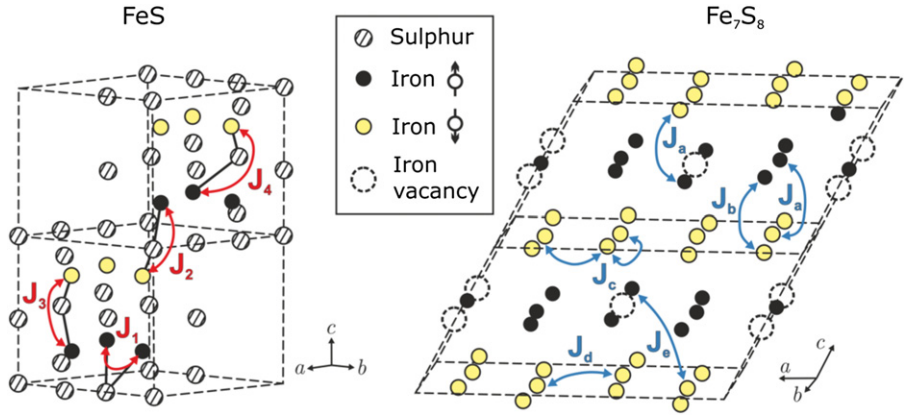

Figure 7. Schematic representation of the crystal lattice of FeS troilite and Fe_7S_8 pyrrhotite together with the strongest magnetic interaction pathways identified using DFT + U. The numbering is done in an arbitrary manner.

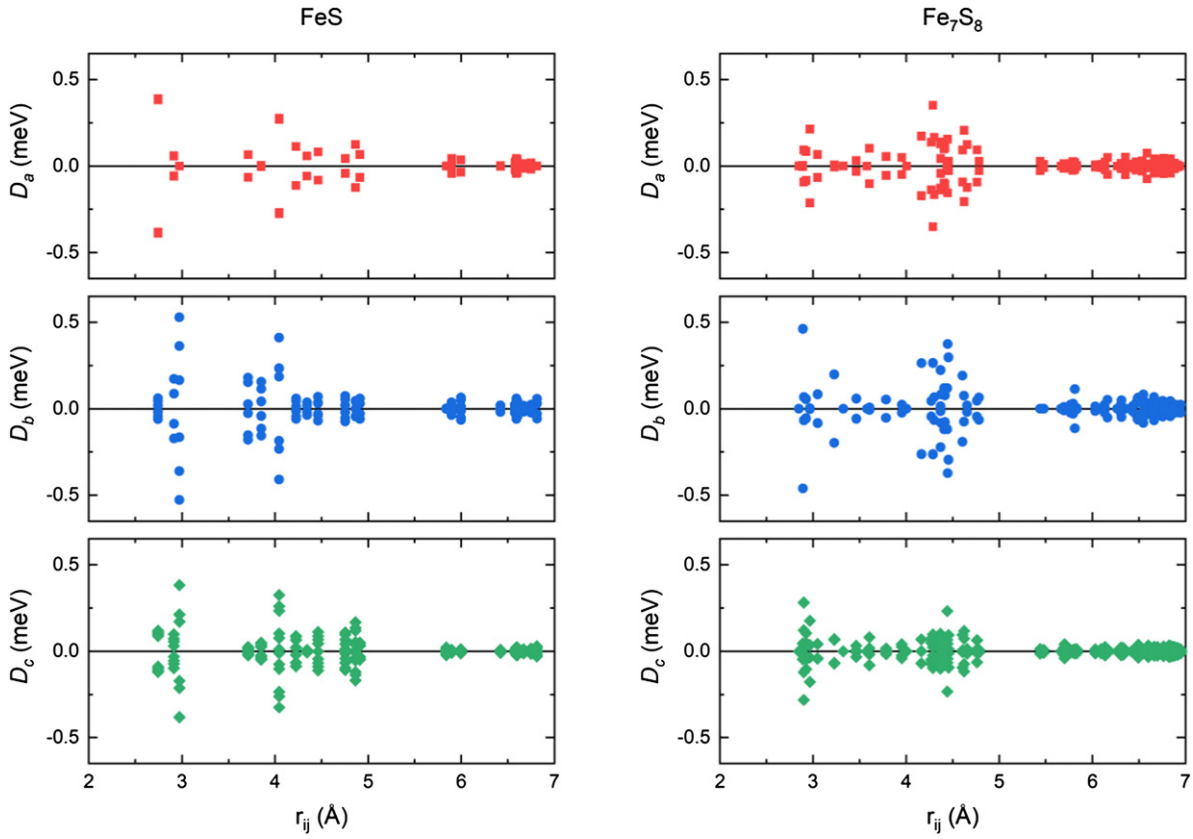

Figure 8. DM vector components along the a, b, c direction of FeS and Fe_7S_8, as a function of interatomic distance, obtained with TB2J using DFT + U + SOC.

The DFT + U + SOC calculated parameters of the DM vectors for both FeS and Fe_7S_8 are shown in figure 8. The components of the strongest magnetic interactions are listed in table 2. There is no clear observable trend among the different DM components, neither for FeS nor Fe_7S_8. The largest magnitude of the DM vector reads 0.65 meV or FeS (2.3% of the J_3 interaction) and 0.38 meV (1.8% of the J_a interaction) for Fe_7S_8. The canting angles, in competition with the isotropic collinear Heisenberg exchange (estimated through the relation $|D_{ij}|/|J_{ij}|$), are calculated to be 1.318° and 1.661° for the strongest FM and AFM interaction in FeS, respectively. The canting angles between spin pairs in Fe_7S_8 are decreased when compared to FeS and estimated at 0.515° and 0.802° for the most prominent FM and AFM interactions, respectively. When compared to materials which possess helical cycloid phases or skyrmionics states, where the D/J ratio is typically in the range of 0.1–0.2 [66, 67], the DM interaction in troilite and 4C pyrrhotite induces fairly weak effects.

Finally, it should be noted that the outlined results obtained using DFT + U are only able to partially account for

Table 2. Calculated components of the DM interaction vector for strongest interactions between magnetic Fe atoms in FeS and Fe_7S_8 as identified earlier.

	D_a	D_b	D_c	$\|D\|$	J
FeS	−0.383	0.044	−0.088	0.395	$J_1 = 16.5$
	−0.060	−0.086	−0.031	0.110	$J_2 = -16.4$
	0.000	−0.528	−0.383	0.652	$J_3 = -22.3$
	0.276	0.233	0.234	0.430	$J_4 = -17.5$
Fe_7S_8	−0.049	−0.197	−0.118	0.384	$J_a = -21.2$
	−0.213	−0.003	0.036	0.216	$J_b = -16.9$
	−0.050	−0.010	−0.003	0.075	$J_c = 8.7–12.3$
	−0.007	0.197	0.071	0.209	$J_d = -8.5$
	−0.016	0.052	0.041	0.259	$J_e = -13.7$

the strong electron correlation present in systems such as pyrrhotites. Despite good agreement with experimentally available data, additional research using methods including improved description of electron correlation, such as DFT + DMFT, would be desirable to further verify the validity of the results outline in this work.

4. Conclusion

In this work, the origin of the magnetic interactions appearing in two end members of the pyrrhotite group of iron sulphide materials has been analysed by means of DFT calculations. The strongest interaction is found to occur between nearest neighbouring iron atoms favouring AFM spin alignment between iron layers along the crystallographic *c*-plane and ferromagnetic alignment between iron atoms within the same layer in the *ab*-plane. The high symmetrical structure of FeS implies an overall net zero moment across the unit cell, while the low symmetry structure of Fe_7S_8 exhibits ferrimagnetism as a result of the uncompensated magnetic moment in the iron-vacancy rich layers. Comparing the two systems, the ferromagnetic intra-layer iron interaction in Fe_7S_8 is weakened in comparison to FeS, while the AFM inter-layer interactions remain almost unaltered. Calculated values compare well with experimental values when available and provide fundamental complementary information. The DFT + U method is confirmed as suitable for modelling the ground state properties of pyrrhotite group members.

Acknowledgments

AZ and NHdL acknowledge the NWO ECHO Grant (712.018.005) for funding. Part of the local compute cluster and the research work of MW is part of the Industrial Partnership Programme i32 Computational Sciences for Energy Research that is carried out under an agreement between Shell and the Netherlands Organisation for Scientific Research (NWO). This project has received funding from the European Research Council (ERC) under the European Union's Horizon 2020 research and innovation programme (Grant agreement No. 819588). This work was carried out on the Dutch national e-infrastructure with the support of SURF Cooperative. The authors would also like to thank Xu He and Eric Bousquet for explaining the limitations of the Heisenberg model and technical support with TB2J.

Data availability statement

All data that support the findings of this study are included within the article (and any supplementary files).

ORCID iDs

Aleksandar Živković https://orcid.org/0000-0003-1347-6203
Mariette Wolthers https://orcid.org/0000-0003-3908-5622

References

[1] Néel L 1953 Some new results on antiferromagnetism and ferromagnetism *Rev. Mod. Phys.* **25** 58–63
[2] Krontiras C, Pomoni K and Theodossiou A 1984 Resistivity anisotropy of pyrrhotite *J. Appl. Phys.* **55** 3894–5
[3] Kind J, García-Rubio I, Charilaou M, Nowaczyk N R, Löffler J F and Gehring A U 2013 Domain-wall dynamics in 4C pyrrhotite at low temperature *Geophys. J. Int.* **195** 192–9
[4] de Villiers J P R and Liles D C 2010 The crystal-structure and vacancy distribution in 6C pyrrhotite *Am. Mineral.* **95** 148–52
[5] Wang H and Salveson I 2005 A review on the mineral chemistry of the non-stoichiometric iron sulphide, $Fe_{1-x}S$ ($0 \leqslant x \leqslant 0.125$): polymorphs, phase relations and transitions, electronic and magnetic structures *Phase Transit.* **78** 547–67
[6] Takele S and Hearne G R 2001 Magnetic-electronic properties of FeS and Fe_7S_8 studied by ^{57}Fe Mössbauer and electrical measurements at high pressure and variable temperatures *J. Phys.: Condens. Matter* **13** 10077–88
[7] Kavner A, Duffy T S and Shen G 2001 Phase stability and density of FeS at high pressures and temperatures: implications for the interior structure of Mars *Earth Planet. Sci. Lett.* **185** 25–33
[8] Martín-Hernández F, Dekkers M J, Bominaar-Silkens I M A and Maan J C 2008 Magnetic anisotropy behaviour of pyrrhotite as determined by low- and high-field experiments *Geophys. J. Int.* **174** 42–54
[9] Rickard D and Luther G W 2007 Chemistry of iron sulfides *Chem. Rev.* **107** 514–62
[10] Shimada K *et al* 1998 Spin-integrated and spin-resolved photoemission study of Fe chalcogenides *Phys. Rev.* B **57** 8845–53
[11] Ovanesyan N S, Trukhtanov V A, Odinets G Y and Novikov G V 1971 Vacancy distribution and magnetic ordering in iron sulfides *Sov. Phys. JETP-USSR* **3** 1193–7
[12] Sato K 1966 Magnetizing process of pyrrhotite crystal in high magnetic field *J. Phys. Soc. Japan* **21** 733–7
[13] Levinson L M and Treves D 1968 Mössbauer study of the magnetic structure of Fe_7S_8 *J. Phys. Chem. Solids* **29** 2227–31
[14] Powell A V, Vaqueiro P, Knight K S, Chapon L C and Sánchez R D 2004 Structure and magnetism in synthetic pyrrhotite Fe_7S_8: a powder neutron-diffraction study *Phys. Rev.* B **70** 014415
[15] Charilaou M, Kind J, Koulialias D, Weidler P G, Mensing C, Löffler J F and Gehring A U 2015 Magneto-electronic coupling in modulated defect-structures of natural $Fe_{1-x}S$ *J. Appl. Phys.* **118** 083903
[16] Koulialias D, Kind J, Charilaou M, Weidler P G, Löffler J F and Gehring A U 2016 Variable defect structures cause the

magnetic low-temperature transition in natural monoclinic pyrrhotite *Geophys. J. Int.* **204** 961–7
[17] Koulialias D, Canévet E, Charilaou M, Weidler P G, Löffler J F and Gehring A U 2018 The relation between local structural distortion and the low-temperature magnetic anomaly in Fe_7S_8 *J. Phys.: Condens. Matter* **30** 425803
[18] Volk M W R, McCalla E, Voigt B, Manno M, Leighton C and Feinberg J M 2018 Changes in physical properties of 4C pyrrhotite (Fe_7S_8) across the 32 K Besnus transition *Am. Mineral.* **103** 1674–89
[19] Koulialias D, Schäublin R, Kurtuldu G, Weidler P G, Löffler J F and Gehring A U 2018 On the magnetism behind the Besnus transition in monoclinic pyrrhotite *J. Geophys. Res. Solid Earth* **123** 6236–46
[20] Koulialias D, Lesniak B, Schwotzer M, Weidler P G, Löffler J F and Gehring A U 2019 The Besnus transition in single-domain 4C pyrrhotite *Geochem. Geophys. Geosyst.* **20** 5216–24
[21] Haines C R S, Dutton S E, Volk M W R and Carpenter M A 2020 Magnetoelastic properties and behaviour of 4C pyrrhotite, Fe_7S_8, through the Besnus transition *J. Phys.: Condens. Matter* **32** 405401
[22] William Herbert F, Krishnamoorthy A, Rands L, van Vliet K J and Yildiz B 2015 Magnetic diffusion anomaly at the Néel temperature of pyrrhotite, $Fe_{1-x}S$ *Phys. Chem. Chem. Phys.* **17** 11036–41
[23] Herbert F W, Krishnamoorthy A, Yildiz B and van Vliet K J 2015 Diffusion-limited kinetics of the antiferromagnetic to ferrimagnetic λ-transition in $Fe_{1-x}S$ *Appl. Phys. Lett.* **106** 092402
[24] Nath M, Choudhury A, Kundu A and Rao C N R 2003 Synthesis and characterization of magnetic iron sulfide nanowires *Adv. Mater.* **15** 2098–101
[25] Takayama T and Takagi H 2006 Phase-change magnetic memory effect in cation-deficient iron sulfide $Fe_{1-x}S$ *Appl. Phys. Lett.* **88** 012512
[26] Shirai M, Suzuki N and Motizuki K 1996 Electronic band structure and photoemission spectra of Fe_7S_8 *J. Electron Spectrosc. Relat. Phenom.* **78** 95–8
[27] Becker U, Munz A W, Lennie A R, Thornton G and Vaughan D J 1997 The atomic and electronic structure of the (001) surface of monoclinic pyrrhotite (Fe_7S_8) as studied using STM, LEED and quantum mechanical calculations *Surf. Sci.* **389** 66–87
[28] Martin P, Price G D and Vočadlo L 2001 An *ab initio* study of the relative stabilities and equations of state of FeS polymorphs *Mineral. Mag.* **65** 181–91
[29] Wells S, Alfe D, Blanchard L, Brodholt J, Calleja M, Catlow R, Price D, Tyler R and Wright K 2005 *Ab initio* simulations of magnetic iron sulphides *Mol. Simul.* **31** 379–84
[30] Ricci F and Bousquet E 2016 Unveiling the room-temperature magnetoelectricity of troilite FeS *Phys. Rev. Lett.* **116** 1–5
[31] Antonov V N, Bekenov L V, Shpak A P, Germash L P, Yaresko A N and Jepsen O 2009 X-ray magnetic circular dichroism in iron chalcogenides $Fe_{1-x}S$: first-principles calculations *J. Appl. Phys.* **106** 123907
[32] Ushakov A V, Shorikov A O, Anisimov V I, Baranov N V and Streltsov S V 2017 Suppression of magnetism under pressure in FeS: a DFT + DMFT study *Phys. Rev.* B **95** 205116
[33] Kresse G and Joubert D 1999 From ultrasoft pseudopotentials to the projector augmented-wave method *Phys. Rev.* B **59** 1758–75
[34] Kresse G and Furthmüller J 1996 Efficient iterative schemes for *ab initio* total-energy calculations using a plane-wave basis set *Phys. Rev.* B **54** 11169–86
[35] Kresse G and Furthmüller J 1996 Efficiency of *ab initio* total energy calculations for metals and semiconductors using a plane-wave basis set *Comput. Mater. Sci.* **6** 15–50
[36] Perdew J P, Burke K and Ernzerhof M 1996 Generalized gradient approximation made simple *Phys. Rev. Lett.* **77** 3865–8
[37] Dudarev S L, Botton G A, Savrasov S Y, Humphreys C J and Sutton A P 1998 Electron-energy-loss spectra and the structural stability of nickel oxide: an LSDA + U study *Phys. Rev.* B **57** 1505–9
[38] Rohrbach A, Hafner J and Kresse G 2003 Electronic correlation effects in transition-metal sulfides *J. Phys.: Condens. Matter* **15** 979–96
[39] Grimme S, Antony J, Ehrlich S and Krieg H 2010 A consistent and accurate *ab initio* parametrization of density functional dispersion correction (DFT-D) for the 94 elements H-Pu *J. Chem. Phys.* **132** 154104
[40] Monkhorst H J and Pack J D 1976 Special points for Brillouin-zone integrations *Phys. Rev.* B **13** 5188–92
[41] Yu M and Trinkle D R 2011 Accurate and efficient algorithm for Bader charge integration *J. Chem. Phys.* **134** 064111
[42] Tang W, Sanville E and Henkelman G 2009 A grid-based Bader analysis algorithm without lattice bias *J. Phys.: Condens. Matter* **21** 084204
[43] Sanville E, Kenny S D, Smith R and Henkelman G 2007 Improved grid-based algorithm for Bader charge allocation *J. Comput. Chem.* **28** 899–908
[44] Momma K and Izumi F 2011 VESTA 3 for three-dimensional visualization of crystal, volumetric and morphology data *J. Appl. Crystallogr.* **44** 1272–6
[45] Liechtenstein A I, Katsnelson M I, Antropov V P and Gubanov V A 1987 Local spin density functional approach to the theory of exchange interactions in ferromagnetic metals and alloys *J. Magn. Magn. Mater.* **67** 65–74
[46] Daalderop G H O, Kelly P J and Schuurmans M F H 1991 Magnetocrystalline anisotropy and orbital moments in transition-metal compounds *Phys. Rev.* B **44** 12054–7
[47] Pizzi G *et al* 2020 Wannier90 as a community code: new features and applications *J. Phys.: Condens. Matter* **32** 165902
[48] Souza I, Marzari N and Vanderbilt D 2001 Maximally localized Wannier functions for entangled energy bands *Phys. Rev.* B **65** 35109
[49] Marzari N and Vanderbilt D 1997 Maximally localized generalized Wannier functions for composite energy bands *Phys. Rev.* B **56** 12847–65
[50] Marzari N, Mostofi A A, Yates J R, Souza I and Vanderbilt D 2012 Maximally localized Wannier functions: theory and applications *Rev. Mod. Phys.* **84** 1419–75
[51] He X, Helbig N, Verstraete M J and Bousquet E 2021 TB2J: a python package for computing magnetic interaction parameters *Comput. Phys. Commun.* **264** 107938
[52] Makovicky E 2006 Crystal structures of sulfides and other chalcogenides *Rev. Mineral. Geochem.* **61** 7–125
[53] Coey J M D and Roux-Buisson H 1979 Electronic properties of $(Ni_{1-x}Fe_x)$s solid solutions *Mater. Res. Bull.* **14** 711–6
[54] Fillion G, Mattei J L, Rochette P and Wolfers P 1992 Neutron study of 4C pyrrhotite *J. Magn. Magn. Mater.* **104–107** 1985–6
[55] Martin R M 2004 *Electronic Structure* (*Basic Theory and Practical Methods*) (Cambridge: Cambridge University Press)
[56] Hobbs D and Hafner J 1999 Magnetism and magneto-structural effects in transition-metal sulphides *J. Phys.: Condens. Matter* **11** 8197–222
[57] Pearce C I 2006 Electrical and magnetic properties of sulfides *Rev. Mineral. Geochem.* **61** 127–80
[58] Andresen A F, Hofman-Bang N, Bak T A, Varde E and Westin G 1960 Magnetic phase transitions in stoichiometric FeS studied by means of neutron diffraction *Acta Chem. Scand.* **14** 919–26
[59] Koulialias D, Charilaou M, Schäublin R, Mensing C, Weidler P G, Löffler J F and Gehring A U 2018 Ordered defects in

$Fe_{1-x}S$ generate additional magnetic anisotropy symmetries *J. Appl. Phys.* **123** 033902
[60] Goodenough J B 1962 Cation–Cation three-membered ring formation *J. Appl. Phys.* **33** 1197–9
[61] Anderson P W 1950 Antiferromagnetism. Theory of superexchange interaction *Phys. Rev.* **79** 350–6
[62] Kanamori J 1957 Theory of the magnetic properties of ferrous and cobaltous oxides, I *Prog. Theor. Phys.* **17** 177–96
[63] Goodenough J B 1967 Narrow-band electrons in transition-metal oxides *Czech. J. Phys.* **17** 304–36
[64] Goodenough J B 1958 An interpretation of the magnetic properties of the perovskite-type mixed crystals $La_{1-x}Sr_xCoO_{3-\lambda}$ *J. Phys. Chem. Solids* **6** 287–97
[65] Khomskii D I 2014 *Transition Metal Compounds* (Cambridge: Cambridge University Press)
[66] Li X, Yu H, Lou F, Feng J, Whangbo M H and Xiang H 2021 Spin Hamiltonians in magnets: theories and computations *Molecules* **26** 1–26
[67] Kim B H and Min B I 2011 Effect of orbital symmetry on the anisotropic superexchange interaction *New J. Phys.* **13** 073034